Space Weather

RESEARCH ARTICLE
10.1029/2018SW002119

Estimation of Spatial Gradients and Temporal Variations of the Total Electron Content Using Ground-Based GNSS Measurements

N. Jakowski[1] and M. M. Hoque[1]

[1]Institute of Communications and Navigation, German Aerospace Center (DLR), Neustrelitz, Germany

Key Points:
- The new method enables characterizing spatial gradients of the total electron content derived from GNSS data
- The new method enables characterizing rapid ionospheric changes of the total electron content derived from GNSS data
- Derived quantities are able to characterize the instantaneous perturbation degree of the ionosphere by indices usable in space weather services

Correspondence to:
N. Jakowski,
norbert.jakowski@dlr.de

Citation:
Jakowski, N., & Hoque, M. M. (2019). Estimation of spatial gradients and temporal variations of the total electron content using ground-based GNSS measurements. *Space Weather*, *17*. https://doi.org/10.1029/2018SW002119

Received 11 NOV 2018
Accepted 7 FEB 2019
Accepted article online 11 FEB 2019

Abstract Precision and safety of life applications of Global Navigation Satellite Systems require key information on space weather conditions in particular on the perturbation degree of the ionosphere. Such systems are particularly vulnerable against severe spatial gradients and rapid changes of the total electron content (TEC) measured along different satellite-receiver links. To estimate spatial gradients and rapid temporal variations of ionospheric TEC, two approaches are discussed. The Gradient Ionosphere indeX (GIX) and the Sudden Ionospheric Disturbance indeX are able to estimate the perturbation degree of the ionosphere instantaneously without taking into account previous measurements. The capabilities and accuracy of the index approaches are demonstrated by simulations using a 3-D electron density model of the ionosphere and plasmasphere in conjunction with realistic Global Navigation Satellite Signal constellations. Real data tests confirm the applicability of GIX and the related standard deviation GIX Sigma to monitor spatial gradients. Sudden Ionospheric Disturbance indeX is able to monitor rapid temporal variations of TEC as exemplified by using Global Navigation Satellite Signal measurements carried out during solar flare events. Both approaches could identify enhanced space weather impacts on precise point positioning and the European Geostationary Navigation Overlay Service. More comprehensive studies analyzing ionospheric storms in close dialogue with potential customers are needed to fully utilize the potential of these approaches to serve as objective ionospheric indices for scaling horizontal TEC gradients and rapid TEC variations in space weather services.

Plain Language Summary Modern telecommunication and navigation systems may be heavily disturbed by charged particles of the Earth's ionosphere like electrons and ions. These important technological systems may fail due to degradation or even loss of signals during severe perturbations of the ionospheric plasma initiated by severe space weather events. In this paper two methods are described which provide instantaneous information on the perturbation degree of the ionosphere after analyzing continuously transmitted signals from Global Navigation Satellite Signals (GNSS). The data are available via numerous national and international GNSS receiver networks and serve to derive the Total Electron Content of the ionosphere. Using this quantity, spatial gradients and rapid temporal variations of ionospheric Total Electron Content can be estimated in two different approaches over a predefined region. The Gradient Ionosphere indeX and the Sudden Ionospheric Disturbance indeX are able to characterize the spatial and temporal perturbation degree of the ionosphere instantaneously without taking into account previous measurements. The applicability of these indices has been simulated and tested by using GNSS data obtained over Europe. The proposed indices which could easily be distributed via space weather services should be well suited to reducing safety and accuracy risks in GNSS navigation and positioning.

1. Introduction

Ionospheric perturbations can adversely affect the accuracy, continuity, availability, and integrity of modern Global Navigation Satellite Systems (GNSS) in different ways. Thus, reliable information on key parameters describing the perturbation degree of the ionosphere is important to guarantee the required safety level, for example, in Ground-Based Augmentation Systems (GBAS) and Satellite-Based Augmentation Systems (SBAS) established for GNSS based aircraft landing. Such systems are vulnerable to severe spatial (horizontal) gradients and rapid changes of the electron density integrated along ray paths called slant Total Electron Content (STEC). Due to the dispersive nature of the ionospheric plasma, the ionospheric impact, measurable as time delay or range error in GNSS applications, can be derived from differential phase measurements of coherent dual frequency GNSS signals.

As our knowledge on the spatial and temporal variations of the ionosphere is permanently incomplete, it would be helpful to have proxy information for key parameters of the ionospheric state similar to how the level of geomagnetic activity is estimated by indices like Kp, Ap, or Dst. Although such an index will not be able to describe the exact propagation conditions at the measurement site, a powerful ionospheric index could be helpful to estimate the probability of violating required accuracy bounds or protection levels in diverse GNSS applications. Thus, aircraft landing via GBAS require an ionospheric threat model that describes worst-case gradients of TEC (e.g., Mayer et al., 2009; Pullen et al., 2009; Saito et al., 2017). On the other hand, extreme rapid changes of the GNSS signal phase might cause loss of lock at the receiver level as was observed during the big solar flare on 28 October 2003 in conjunction with the severe Halloween storm (Jakowski, 2017). As all GNSS measurements represent a mix of the spatial and temporal variability of the ionosphere, it is difficult to distinguish between both effects without TEC mapping (Jakowski et al., 2005). To overcome this problem, Jakowski, Borries, et al. (2012) proposed a so-called Disturbance Ionosphere Index (DIX) that is able to separate horizontal TEC gradient effects and rapid TEC changes in near real-time. A slightly modified DIX approach has been shown to be able to describe the regional and global perturbations via spatial gradients of TEC (Wilken et al., 2018). This paper presents a study for demonstrating another modification of the original DIX concept that enables the estimation of absolute values of spatial gradients and temporal changes of TEC. Such immediate and concrete information is essential for safe navigation and precise positioning applications. Compared with other indices which collect data over time intervals from several minutes (Pi et al., 1997) up to 1 hr like the Along Arc TEC Rate (AATR) index (Sanz et al., 2014) to statistically define an index value, the DIX approach is able to provide actual information with a time delay of less than 1 min.

A fast and actual estimation of horizontal gradients of TEC is important to warn users because extreme gradients may significantly degrade the safety of navigation solutions and limit the accuracy in precise positioning. The most up-to-date information on the ionospheric state is also needed to predict the behavior of TEC and its dynamic. The ionospheric threat model boundaries for spatial gradients utilized for safe aircraft landing via GBAS range from 200 mm/km or approximately 1 TECU/km (Mayer et al., 2009) to more than 400 mm/km or approximately 2 TECU/km (Pullen et al., 2009) and even to more than 600 mm/km (≈3 TECU/km; Pradipta & Doherty, 2016; Saito et al., 2017). Thus, for an aircraft at 6-km distance from the airport, the maximum ionosphere error in vertical ranges up to 20 m when considering the threat model for Germany that defines equivalent overbounds of approximately 250 up to 860 mTECU/km (1 mTECU/km = 10^{-3}TECU/km) for low and high elevation angles, respectively (Mayer et al., 2009). It should be mentioned that hereinafter gradient values are presented in a generalized form, that is, in milliTEC units per kilometer instead of millimeters per kilometer because range errors depend on the frequency used which may be different from L1 frequency used in the above mentioned studies. These gradient numbers represent worst-case scenarios derived from real observations during severe storms, like the Halloween storm, in different geographic regions and particularly at low latitudes. To derive immediate information on TEC gradients, the DIX concept presented here is applied focusing on the use of calibrated STEC data. At present, the bias determination for calibrating GNSS-based TEC measurements achieves accuracy in the order of ±1 TECU. Our study will demonstrate how accurate gradients can be estimated when applying the proposed approach.

This paper exclusively uses GNSS data for studying options suitable for defining ionospheric indices, even though other types of ionospheric measurement techniques (e.g., vertical sounding or incoherent scatter) significantly contribute to ionospheric sounding. There are several reasons for this. Well-established global ground-based dual frequency GNSS networks are able to provide ionospheric TEC information in near real-time via Networked Transport of Radio Technical Commission for Maritime Services via Internet Protocol (NTRIP) technology (Weber et al., 2005), and also, there are numerous dense networks like International GNSS Service (IGS) and European Geodetic Reference System (EUREF) that are publicly available. Besides, despite the continued growth of these networks, the number of GNSS satellites belonging to different systems such as GPS and Globalnaja Nawigazionnaja Sputnikowaja Sistema (GLONASS) also continues to increase parallel to the completion of systems like Galileo and Beidou. The data are continuously available with a high time resolution of 1 s or even higher at scintillation monitoring sites. Another argument underlining the use of GNSS data is the fact that GNSS users are impacted by ionospheric perturbations and need up-to-date and user-friendly information on the current and predicted state of the ionosphere.

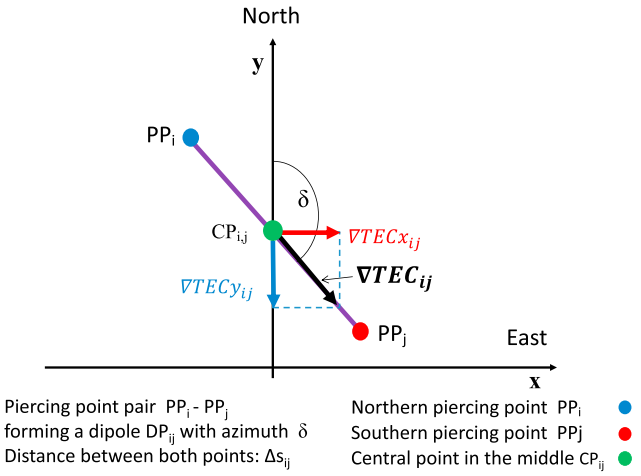

Figure 1. Graphic showing the station pair derived terms used in the paper. TEC = total electron content.

2. Basic Equations for Estimating Spatial and Rapid Temporal Variations of TEC

The estimation of spatial gradients of ionospheric TEC is based on dual frequency GNSS measurements providing a measure of calibrated STEC along numerous satellite-receiver links (Jakowski, Mayer, et al., 2011). Satellite-receiver links moving through the ionosphere and providing the STEC along the ray path are taken into consideration. Conversion of the link-related STEC to the vertical TEC is made by using a mapping function M, for example, by the spherical single layer mapping function M (Hoque et al., 2014). To keep the notation straightforward, TEC = vertical TEC is set in the following and the STEC is defined by

$$STEC = M \cdot TEC. \tag{1}$$

Assuming a residual error of differential code bias estimation and measurement noise ΔB, the following is given for the vertical TEC at each satellite-receiver link

$$TEC = \frac{STEC \pm \Delta B}{M}. \tag{2}$$

To derive TEC gradients and temporal variations of TEC from GNSS measurement data, pairs of ionospheric piercing points are considered in line with Jakowski, Borries, et al. (2012) who included all possible receiver-satellite configurations to derive TEC gradients as in case of the Mixed-Pair method which differs from the Station-Pair and Time-Step methods (cf. Lee et al., 2006; Pradipta & Doherty, 2016). The Station-Pair method only utilizes measurements of receiver pairs receiving the same GNSS satellite, and the Time-Step or Single-Station method derives gradients from TEC changes between subsequent epochs along the satellite tracks observed at the considered single receiver in question. Whereas the Station-Pair and Mixed-Pair methods suffer from calibration errors of STEC, the Single-Station method is not able to distinguish between spatial and temporal variations because it utilizes data points from consecutive epochs (Lee et al., 2006; Pradipta & Doherty, 2016). This paper will show that our method which considers all receiver-satellite configurations reduces the problem of calibration errors due to a much better statistical database at any time of measurement.

The basic relationships of two ionospheric piercing points used here are shown in Figure 1. As the direction of the axis between both ionospheric piercing points is taken into consideration here, such a piercing point pair (PP_i-PP_j) is denoted as dipole DP_{ij}. The angle δ defines the azimuth of the TEC gradient vector along the dipole axis. The distance between both points is Δs_{ij}; the central point between the pair PP_i-PP_j is CP_{ij}.

2.1. Spatial Gradients

The TEC gradient value between piercing points PP_j and PP_i is defined by

$$\nabla TEC_{ij} = \left(\frac{STEC_i \pm \Delta B_i}{M_i} - \frac{STEC_j \pm \Delta B_j}{M_j}\right) \cdot \frac{1}{\Delta s_{ij}}. \tag{3}$$

In the following, $\nabla \boldsymbol{TEC_{ij}}$ denotes the gradient vector and ∇TEC_{ij} for the measured gradient value. It is assumed that the bias error is very similar at all receiver-satellite links for receivers located in the same region such as the European region, approximately in the order of $\Delta B_i \approx \Delta B_j \leq 1$ TECU which is the state-of-the-art in terms of estimating differential code biases (e.g., Montenbruck et al., 2014). This results in the following for ∇TEC_{ij}

$$\nabla TEC_{ji} = \left(\frac{STEC_i}{M_i} - \frac{STEC_j}{M_j}\right) \cdot \frac{1}{\Delta s_{ij}} \pm \frac{M_j - M_i}{M_i \cdot M_j} \cdot \frac{\Delta B}{\Delta s_{ij}}. \tag{4}$$

As the second part of the equation indicates, problems in estimating gradients might occur at small piercing point distances and large TEC calibration errors ΔB. Assuming a bias error of approximately 1 TECU at a

minimum distance Δs_{ij} of 30 km which will be used in this paper, an ionospheric gradient error of approximately 44 mTECU/km or 7 mm/km at L1 frequency may occur in worst-case conditions. Nevertheless, this value is not crucial for Safety of Life applications, but it is greater than gradients observed in the regular mid-latitude ionosphere in the order of 1–3 mm/km (Lee et al., 2006). Considering the statistics over selected measurements, it is expected that the final estimates are much more accurate as will be shown in section 3.1.1. Thus, gradient estimates during ionospheric storms becoming crucial at approximately 25–30 mm/km at L1 should be applicable in operational space weather services for customers. In particular, the impact is small if $\left|\frac{M_i - M_i}{M_i \cdot M_j}\right| \ll 1$ in equation (4). This is valid if data from only one GNSS satellite and different ground stations are used in a country with a lateral extension of less than 1,000 km, like Germany (cf. Wilken et al., 2018).

Gradients are directed along the dipole axis (positive toward North) and located at the central dipole point CP_{ij}. From such dipole values, an average gradient value can be computed based on all dipoles included in the computation. The maximum number N_D of dipoles that can be included in a selected area containing N piercing points is given by

$$N_D = N \cdot (N-1)/2. \tag{5}$$

The TEC gradient vector $\nabla \boldsymbol{TEC_{ij}}$ can be split into a meridional (northward) component

$$\nabla TECy_{ij} = \frac{\partial TEC_{ij}}{\partial y}, \tag{6}$$

and a zonal (eastward) component

$$\nabla TECx_{ij} = \frac{\partial TEC_{ij}}{\partial x}. \tag{7}$$

With the azimuth of the dipole δ and the absolute gradient value $\nabla TEC_{ij} = |\nabla \boldsymbol{TEC_{ij}}|$, the zonal component (West-East) is given by

$$\nabla TECx_{ij} = \nabla TEC_{ij} \cdot \sin\delta, \tag{8}$$

and for the meridional component (South-North)

$$\nabla TECy_{ij} = \nabla TEC_{ij} \cdot \cos\delta. \tag{9}$$

Zonal average over a certain region containing N_C dipoles which fulfill selection criteria such as elevation angle cutoff or dipole length range (i.e., $N_C \le N_D$) can be expressed by

$$\langle \nabla TECx \rangle = \frac{1}{N_C} \sum_{i=1}^{N_C} \nabla TECx_{ij}. \tag{10}$$

Meridional average over a certain region gives

$$\langle \nabla TECy \rangle = \frac{1}{N_C} \sum_{i=1}^{N_C} \nabla TECy_{ij}. \tag{11}$$

The total gradient average is then given by

$$\langle \nabla TEC \rangle = \sqrt[2]{\langle \nabla TECx \rangle^2 + \langle \nabla TECy \rangle^2}. \tag{12}$$

Such a mean value characterizes the overall spatial TEC structure in a certain area but ignores the direction of spatial gradients. Therefore, to avoid loss of information, we prefer to consider the zonal and meridional components separately in our study.

Here we suggest naming referring to the TEC gradients defined in equations (10), (11), and (12) as the Gradient Ionosphere indeX (GIXx, GIXy, GIX) to distinguish it from related DIX approaches which use the calibration independent rate of TEC data (Jakowski, Borries, et al., 2012; Wilken et al., 2018).

The different data sets for $\nabla TECx_{ij}$ and $\nabla TECy_{ij}$ located at CP_{ij} can be mapped in two separate gradient maps to provide some information, for example, on the location and direction of a potential ionospheric front in the course of an ionospheric storm. This can be done in a direct way if sufficient data are available or, for example, by applying the same technique used for TEC mapping (Jakowski, Mayer, et al., 2011).

Gradient maps are useful in GNSS practice to exclude those measurements in the positioning algorithm whose piercing points lie in areas with a high perturbation degree or strong gradients. The disadvantage to mapping total or absolute gradients is that the gradient direction is lost and gradient values are averaged which smooths out extreme values that could eventually be crucial in applications.

Another quantity which can be derived from the actual data set is the dispersion of horizontal TEC gradients in a selected area. This quantity is used in GNSS-based aviation, known as σ_{vig} to quantify the probability of extreme gradients that exceed a fixed protection level (e.g., Lee et al., 2006; Mayer et al., 2009; Pullen et al., 2009; Saito et al., 2017). Taking into account the practical value of this dispersion, we suggest defining a Gradient Ionosphere indeX Sigma (GIXS) by the dispersion of TEC gradients between all the N_C piercing points occurring in a selected area.

The general expression for the dispersion, which also applies separately to the x, y components, is

$$GIXS \equiv \sigma(\nabla TEC) = \sqrt[2]{\left(\langle \nabla TEC^2 \rangle - \langle \nabla TEC \rangle^2\right)}. \tag{13}$$

This computation enables the instantaneous retrieval of information regarding the state of the horizontal gradients of ionospheric ionization.

If no restrictions or selection rules are applied to the data, then the number of PP combinations is $N_C = N_D = N\,(N-1)\,/\,2$. So there are already over 100 values available for 15 PP to compute the dispersion which, even with this small number of values, is already enough to provide a statistical reliability that is not achievable with the classical Station-Pair and Single-Station methods. Further options exist by using multiple values of the dispersion describing stronger confidentiality of the data values.

Another option to estimate the perturbation degree is the use of percentiles of measured gradient distributions. Percentiles are easy to compute which is advantageous in operational near real-time applications. So, following the naming convention introduced here, the related index could be described by $GIXP_{pv}$ where pv refers to the percentage value selected. For this paper, our preference is for $GIXP_{95}$, but any other pv value can be selected according to any specific application requirements.

Principally, GIX, GIXS, and $GIXP_{95}$ can mainly be defined by absolute values (e.g., measured in mTECU/km) or by a dimensionless index that is referred to nominal threshold values (e.g., ∇TEC_T in the order of a few mTECU/km for GIX) that have been found to be representative for the quiet ionosphere. The definition of such thresholds, as suggested by Wilken et al. (2018) for the Disturbance IndeX Spatial Gradient approach, would be a matter for discussion by the international user community in order to define internationally acceptable standards as recently has been discussed at the COSPAR 2018 42nd Assembly in Pasadena, United States (http://cospar2018.org/scientific-program/associated-events/).

If a dimensionless approach is preferred, the current index value must be referred to a threshold value, for example, for GIX this might be

$$GIXr = GIX / \nabla TEC_T, \tag{14}$$

where ∇TEC_T defines a threshold value characterizing the average behavior of TEC gradients over the selected area. For scaling dimensionless spatial and temporal indices, the actual index parameters must primarily refer to basic values characterizing "normal" or "quiet" ionospheric conditions (Wilken et al., 2018). Such basic values should be defined by the international community, standardized, and be valid for all subsequent applications. For the American Wide Area Augmentation System region, the nonstormy or quiet ionosphere is defined by a standard deviation bound of approximately 24 mTECU/km (Lee et al., 2006). For Germany, this quantity has been found to lie in the order of 12 mTECU/km covering all seasons and local times (Mayer et al., 2009). Thus, it becomes clear that this value varies with geographic/geomagnetic location but also might be considered as a function of solar activity and local time. Consequently, the quiet time ionosphere conditions have to be defined carefully for specific applications.

When comparing the applicability of both approaches, the absolute terms GIX, GIXS, or $GIXP_{pv}$ are probably better suited in concrete GNSS applications because the values can be used directly in the algorithms independent of the definition of a reference or threshold value that will change with geophysical conditions as mentioned above. Nevertheless, a dimensionless scale is beneficial for defining an ionospheric weather scale usable in space weather centers alongside the Beaufort force scale, which is used as an empirical measure for describing the strength of tropospheric winds (https://www.metoffice.gov.uk/guide/weather/marine/beaufort-scale).

2.2. Temporal Variations

To characterize the temporal variation of TEC over a certain region, this paper follows Jakowski, Borries, et al. (2012) and utilizes the TEC rate of change. As the bias is assumed to be constant, or at least varies very slowly, the rate of change of the vertical TEC can be derived from equation (2) according to

$$\frac{\Delta TEC}{\Delta t} \approx \frac{1}{M} \frac{\Delta STEC}{\Delta t}. \tag{15}$$

The time derivative of the mapping function M can also be ignored in this context. Here the differential carrier phases of GNSS signals can be used directly as calibration is not needed. To estimate potential error sources in estimating the temporal variation, the total differential of STEC is considered giving

$$\Delta STEC = \frac{\partial STEC}{\partial u} \Delta x + \frac{\partial STEC}{\partial t} \Delta t. \tag{16}$$

Here the u-direction is the direction of the velocity vector $\mathbf{v}$ of the ionospheric piercing point considered

$$\frac{\Delta STEC}{\Delta t} = \frac{\partial STEC}{\partial u} \frac{\Delta x}{\Delta t} + \frac{\partial STEC}{\partial t}. \tag{17}$$

Dividing this expression by the mapping function M gives

$$\frac{\Delta STEC}{M\ \Delta t} = \frac{\partial TEC}{\partial u} v_u + \frac{\partial TEC}{\partial t}. \tag{18}$$

This equation illustrates the well-known fact that the rate of change of TEC includes both temporal and spatial variations of TEC. The temporal variation of TEC is given by

$$\frac{\partial TEC}{\partial t} = \frac{\Delta STEC}{M\ \Delta t} - \frac{\partial TEC}{\partial u} v. \tag{19}$$

The expression $\frac{\partial TEC}{\partial u}$ is identical to the component of the gradient derived in velocity direction $\mathbf{v_u}$. As pointed out by Jakowski, Borries, et al. (2012), the gradient term is at least partially canceled out when averaging the rate of TEC in a selected area. This is due to the fact that the second term in equation (19) may have opposite signs for different satellite-receiver links whose ionospheric piercing points move in different directions. On the other hand, large-scale temporal variations of TEC as observed during a solar flare are recorded at all satellite-receiver links in a similar way with the same sign. When summing up all measurements, the temporal variation is emphasized, and the spatial variation is suppressed in equation (19). So the average of rate of change of TEC measurements can be considered as a proxy for temporal TEC variations in a selected area.

$$\left\langle \frac{\partial TEC}{\partial t} \right\rangle \approx \frac{1}{N} \sum_{i=1}^{N} \left(\frac{\Delta STEC}{M\ \Delta t} \right)_i. \tag{20}$$

The higher the number N of measurements, the better this approach works. The applicability of this approach as an ionospheric index that characterizes large-scale temporal variations of the ionospheric ionization as for instance caused by solar flares is checked using simulation computations in the subsequent section.

2.3. Simulation Study

To demonstrate the capabilities and accuracy of the proposed approaches, TEC gradients and rapid changes of TEC were inserted into a three-dimensional ionosphere model called the Neustrelitz Electron Density Model (NEDM). This model is closely related to a family of ionospheric parameter models that have been developed over the past two decades at the German Aerospace Center (DLR), Institute of Communications and Navigation in Neustrelitz. We developed an empirical global TEC model called the Neustrelitz TEC Model (Jakowski, Hoque, et al., 2011) as well as global models for the ionospheric F2 peak density (NmF2) and height (hmF2) for operational use in radio systems. They are named the Neustrelitz Peak Density Model (Hoque & Jakowski, 2011) and the Neustrelitz Peak Height Model (Hoque & Jakowski, 2012). All these models follow a similar empirical approach describing dependencies on local time, geographic/geomagnetic location, and solar irradiance and activity. Recently, an empirical global plasmasphere model has been added to the Neustrelitz model family. This is called the Neustrelitz Plasmasphere Model (Jakowski & Hoque, 2018) and is used to estimate the topside ionosphere and plasmaspheric density distribution. NEDM is composed of the ionosphere key parameter models Neustrelitz TEC Model, Neustrelitz Peak Density Model, and Neustrelitz Peak Height Model only driven by the solar radio flux index F10.7 that describes the solar activity level. The 3-D approach is realized by combining multiple Chapman layers with a superposed exponential decay function in order to describe the plasmasphere. Using the parameters NmF2, hmF2, and TEC, the Chapman layer can describe the basic structure of the ionosphere. Thus, the model provides the electron density at any time at the entire globe at any height up to the plasmapause height.

An approximate flare simulation is created by superposing a simplified electron density enhancement to the background electron density of NEDM.

Similarly, a realistic ionospheric gradient simulation was realized using an arc tangent function to generate TEC gradients across the geographic latitude. The gradient dynamic was modeled by introducing a slope factor. The phase of the tangent function was considered as the latitude of the desired gradient location. The gradient magnitude was controlled by multiplying the tangent function by an amplitude term. Thus, the TEC variation obtained is only latitude dependent and superposed to the background electron density of NEDM. The measurements simulated were then computed using a realistic GPS constellation. The GPS satellite ephemeris data were taken from a Receiver Independent Exchange Format (RINEX) navigation file for an arbitrary day (1 January 2015). Thirty GPS sensor stations evenly distributed within the European regions 43–48° N latitude and 5–25° E longitude were considered. The actual satellite-to-receiver link geometries were determined every 30 s. The computed STEC values were fed into the proposed flare/gradient detection algorithm as synthetic GNSS measurements. For temporal and spatial gradients detection and analysis, the STEC values were converted to vertical TEC using the thin-shell ionosphere mapping function. To reduce the mapping function related error, the cutoff elevation angle was fixed at 20°.

2.3.1. Estimation of Spatial Gradients

To test the new approaches described in sections 2.1 and 2.2, a latitudinal gradient structure with a TEC enhancement of approximately 20%, the level of a moderate ionospheric storm, was simulated. In case of a solar flare, the TEC enhancement will spread over a large area with small horizontal gradients, typically characterized by a rapid variation of TEC in time as considered in the subsequent section. Large space weather events initiated by coronal mass ejections of the sun can cause extreme gradients of TEC often moving from high toward lower latitudes. In the course of extreme geomagnetic storms like the Halloween storm on 30 October 2003, enhancements of more than 200% have been observed in Europe and over North America (Jakowski, Béniguel, et al., 2012; Mannucci et al., 2005). The simulated South-North gradient is approximately 17 mTECU/km (≈2.8 mm/km) at L1 frequency with a peak at 48° N over Europe as shown in the top panel of Figure 2. Typical quiet time latitudinal variation is about half of this value in this sample. In addition to GIX, GIXS, and $GIXP_{95}$, percentile gradient estimates of meridional ($GIXP_y$) and zonal ($GIXP_x$) components (cf. Figure 1) are introduced here. In considering the components separately, there is an opportunity to distinguish between negative and positive extremes which are associated with the direction of gradients. Whereas in the case of an absolute gradient distribution, only the upper boundary $GIXP_{95}$ is of interest, for component percentiles extreme negative gradients, in this case southward directed, are also of interest. So, instead of expressing $GIXP_{y95}$, the percentile $GIXP_{y95-}$ is used

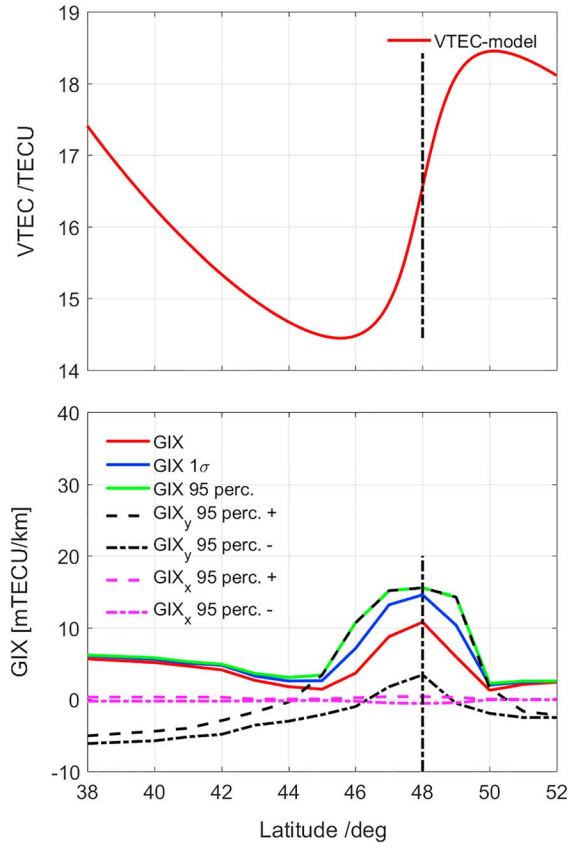

Figure 2. Demonstration of the detectability of a simulated South-North gradient in total electron content at 13:25 UT. (top) Latitudinal dependence of simulated total electron content indicating the gradient peak at 48° N. (bottom) Gradient indices GIX (red), GIXS (blue), $GIXP_{95}$ (green), upper (+) and lower (−) South-North percentiles $GIXP_{y95}$ (black), and upper (+) and lower (−) West-East percentiles $GIXP_{x95}$ (pink). Latitudinal resolution is 1°, indices are averaged zonally over the range 5–25° E. GIX = Gradient Ionosphere indeX; VTEC = vertical total electron content.

for the lower boundary of the North-South component. This means that 95% of gradients are above this extreme negative value $GIXP_{y95-}$ whose absolute value might be greater than its analog $GIXP_{y95+}$ to keep the syntax. This procedure allows the storm mechanism to be studied in greater detail than would be possible if the direction of TEC gradients was ignored as demonstrated in section 3.1.2.

As expected, the peak gradient index GIX (red curve) marks the latitude of the highest slope at 48° N at an average level of 10 mTECU/km which is lower than the modeled value of approximately 17 mTECU/km. Other indices like GIXS and $GIXP_{95}$ reach peak values of approximately 14 and 16 mTECU/km, respectively. Here the role of meridional and zonal components is clearly visible. Whereas $GIXP_{y95+}$ is practically the same as $GIXP_{95}$, the value of $GIXP_{y95-}$ peaks at approximately 3 mTECU/km meaning that there is no negative gradient at the peak location and the average value is around 10 mTECU/km. This is almost the same as GIX as the zonal gradient GIX_x is very small at all latitudes, a priori that was expected given the model input which was mainly South-North. As Figure 2 shows, $GIXP_{y95}$ turns to negative values at latitudes less than approximately 45° N, that is, TEC increases with decreasing latitude which is typical for the climatological daytime behavior of TEC at midlatitudes. It is interesting to note that $GIXP_{y95+}$ and $GIXP_{y95-}$ converge at 38° N at approximately −6 TECU/km, that is, at the same absolute level as indicated by GIX, GIXS, and $GIXP_{95}$ in Figure 2. It becomes clear that the latter indices only consider the absolute gradient values of TEC ignoring the direction of gradients. As in most GNSS applications, the information on current or predicted absolute gradient level is sufficient; GIX, GIXS, and $GIXP_{pv}$ are good candidates for practical use in precise and safety of life applications. The consideration of North-South and East-West components is in particular valuable for scientific studies in order to gain a better insight into storm mechanisms. Hence, both components are included in subsequent real test case studies in section 3.1.

The knowledge of components allows the computation of the direction of an ionospheric front as shown for this simulation in Figure 3 (graphic on right). The gradient information is computed for every 2° in latitude by averaging gradient values at different satellite receiver links over the longitude range 5–25° E.

The propagation vector and the velocity of the ionospheric front can be estimated by monitoring the development of the gradient structure over time. This capability enables the forecasting of the appearance of severe ionospheric fronts, including gradients over a certain area. As such information is important for GNSS users, a related warning service can be established. To inform users on the appearance/approach of

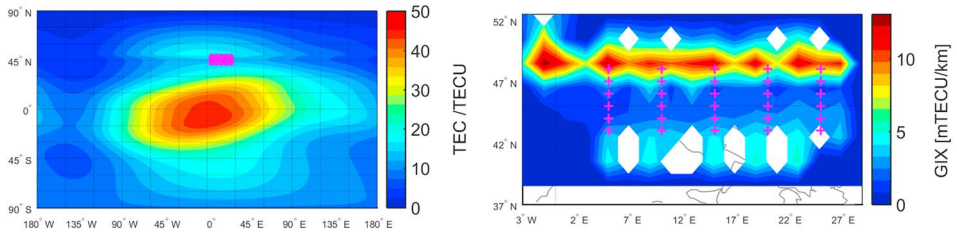

Figure 3. Global map of vertical TEC at 13:15 UT including a latitudinal gradient (left) and derived total TEC gradient distribution over the European region based on simulation studies using Neustrelitz Electron Density Model with a realistic GPS constellation (cf. Figure 2). White areas indicate no data available. TEC = total electron content; GIX = Gradient Ionosphere indeX.

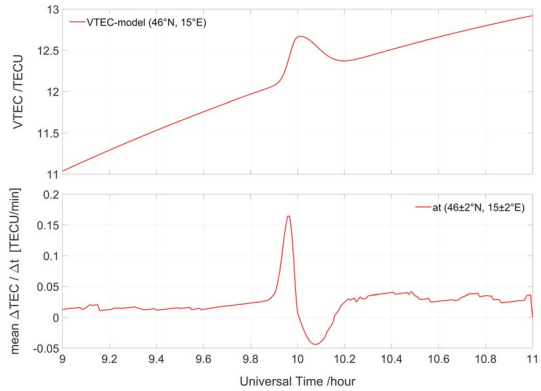

Figure 4. Demonstration of the detection of a simulated rapid temporal variation of TEC (top) by averaging rate of TEC data in a specified area covering the range 44–48° N and 13–17° E (bottom). TEC = total electron content; VTEC = vertical total electron content.

ionospheric gradients in a user-friendly form, we suggest averaging the gradient information (gradient components, total gradient, and dispersion of gradients) for the area of interest. If data coverage is sufficient, actual regional maps of gradient structures can be generated as shown in the right panel in Figure 3. White spots indicate zero data coverage. Data coverage can generally be enhanced by including signals from all GNSS available over a certain area (here only GPS data coverage is considered).

2.3.2. Estimation of SIDs

Besides spatial gradients, rapid temporal changes of the ionospheric ionization, called Sudden Ionospheric Disturbances (SIDs), may also cause problems in navigation and positioning. Thus, the availability of a separate index describing the strength of a SID would be useful for estimating risks concerning safety and accuracy in the navigation and positioning applications of GNSS. To simulate a typical SID, a simple solar flare approach was used in our simulation study.

An approximate flare simulation is realized by combining two Gaussian functions of the type

$$\Delta TEC = A_F \cdot e^{\frac{-(t-t_0)^2}{2\sigma_F^2}}. \tag{21}$$

A_F : Flare amplitude in TEC
σ_F : Flare dynamics
t_0 : Time of flare maximum

This ΔTEC function is simply added to the regular ionosphere provided by the background model. In the subsequent simulation, $A_F = 2$ TECU was fixed under consideration that in reality the amplitude is a function of the solar incidence angle which is ignored here. The increase and decrease time behavior is defined by $\sigma_F(t \le t_0) = 2$ min and $\sigma_F(t \ge t_0) = 5$ min, respectively. The flare peak time is set by $t_0 = 10{:}00$ UT assuming a data sampling interval of $\Delta t = 30$ s.

To estimate the effect of the simulated flare, equation (21) was applied ignoring horizontal gradients which naturally occur. The result can be seen in the top panel in Figure 4 where the flare effect occurs at approximately 10:00 UT characterized by a rapid increase and then a slower decrease of TEC.

Computing the rate change of TEC has been a good option for measuring fast temporal variations for many years. If the solar radiation spectrum is known during a flare, then conclusions can even be drawn on the recombination rate of the ionospheric plasma (Jakowski & Lazo, 1977) or on the solar radiation conditions (Hernández-Pajares et al., 2012). Here the focus is on quantifying the rapid change of TEC over a certain area.

The TEC onset increase during solar flare events is typically faster than the recovery phase when the ionization generated by the flare decreases more slowly in the ionosphere. So the flare detection focuses on the positive peak at flare onset. A more serious argument is that the detection of the onset peak allows near real-time warnings for customers who might be impacted by the flare.

It is suggested that the approach in equation (20) be named “Sudden Ionospheric Disturbance indeX” (SIDX). This index clearly indicates the rate of change of TEC (measured in milliTECU per second) which may impact GNSS applications.

Although spatial gradients are comparatively small in the case of solar flares, the size of the flare effect is different at different sites because the impact depends on the incidence angle of the solar radiation, that is, there is a clear dependence on latitude and local time. Considering this, SIDX should be offered to users for certain regions in near real-time in parallel with GIX.

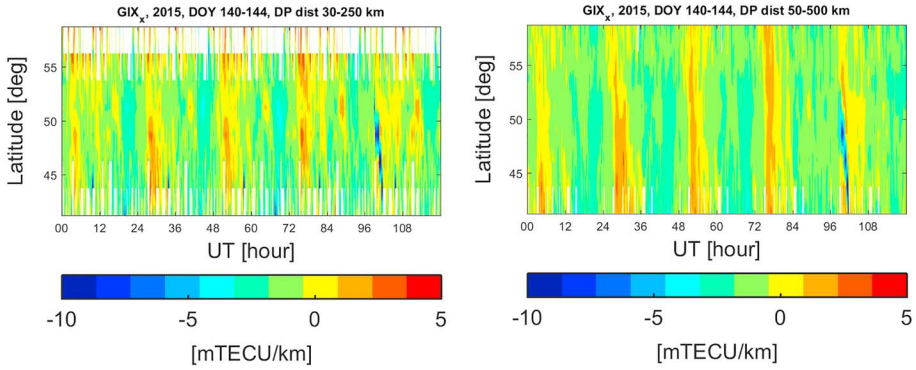

Figure 5. Zonal gradients from 20–25 May 2015 for different dipole lengths $30 \le \Delta s \le 250$ km (left) and $50 \le \Delta s \le 500$ km (right) showing positive values after sunrise before noon increasing toward lower latitudes. Negative values appear in the afternoon and at night as expected. DOY = day of year; GIX = Gradient Ionosphere indeX.

3. Real Data Test Cases

In the following, the suggested approaches are tested by using real data sets obtained at DLR's Ionosphere Monitoring and Prediction Center (IMPC) in Neustrelitz (Berdermann et al., 2014).

3.1. TEC Gradient Estimates

3.1.1. Quiet Ionospheric Conditions

Before considering ionospheric perturbations, the use of suggested indices for the regular ionosphere characterized by small gradients, not crucial to precise and safety of life applications of GNSS, is checked. The results enable the estimation of the impact of bias residuals in equation (4). Preliminary estimates obtained as a by-product of the simulations revealed values of $\Delta M_{ij} = |M_i - M_j| \le 0.2$ at an elevation cutoff angle of 20°. To further reduce the impact of the bias uncertainty, ΔM_{ij} could be restricted to lower values, for example, to

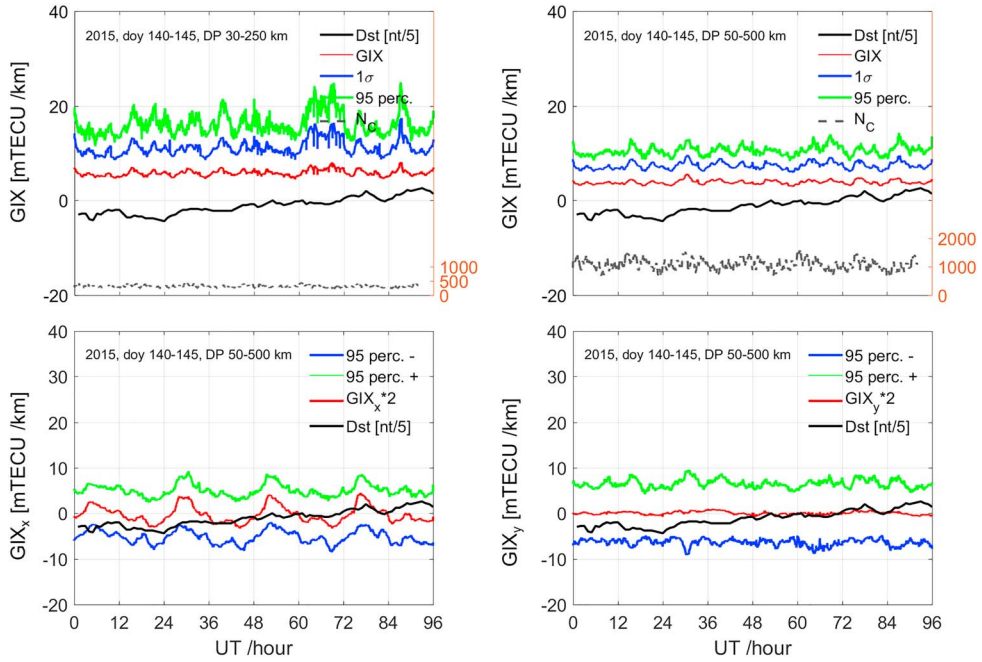

Figure 6. Comparison of $GIX_{x,y}$ and $GIXP_{95\pm}$ over Europe (30–70° N; 20° W–50° E) for West-East components (left panels) South-North (right panels) computed for quiet days 20–25 May 2015. $GIX_{x,y}$ values are multiplied by 2 and the Dst index is divided by 5 for better visibility. The number of dipoles used N_C is plotted at the bottom of the top graphics with the scale shown to the right-hand side. GIX = Gradient Ionosphere indeX.

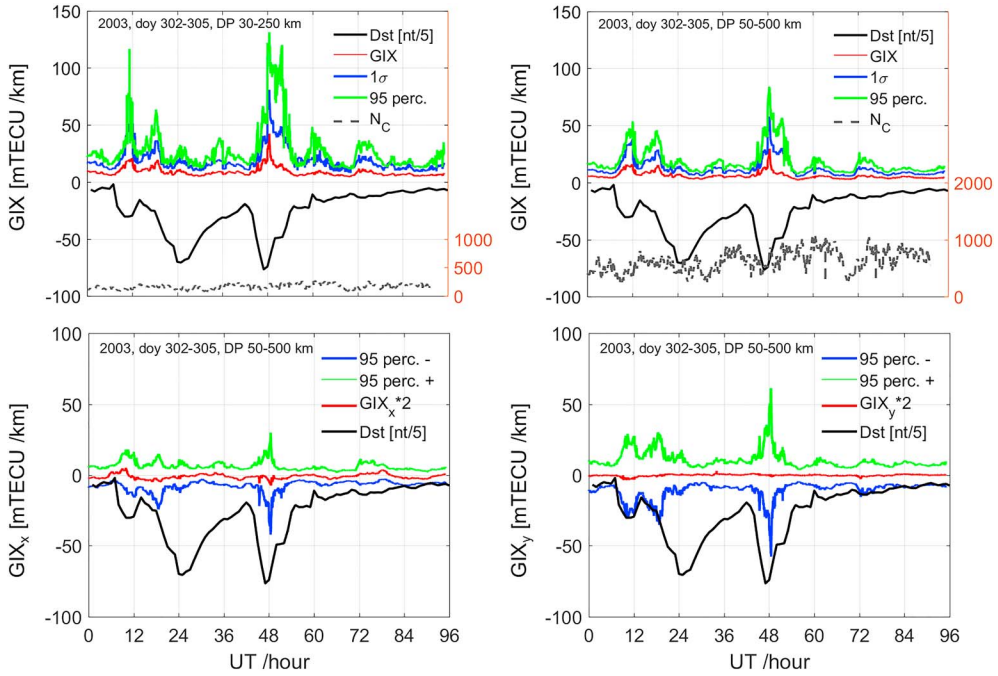

Figure 7. GIX, GIX Sigma, and $GIXP_{95}$ analysis of the Halloween storm on 28 October to 1 November 2003 at ranges 30–250 and 50–500 km (top panels). Components of GIX and $GIXP_{95\pm}$ over Europe (30–70° N; 20° W–50° E) in comparison with the geomagnetic Dst index for 50–500-km range (lower panels). Mean gradient values are multiplied by 2 and the Dst index is divided by 5 for better visibility. GIX = Gradient Ionosphere indeX.

$\Delta M_{ij} \leq 0.1$ by ignoring PP_{ij} with higher ΔM_{ij} values. Considering $M_i \cdot M_j > 1$ and the small bias value ΔB, in the order of 1 TECU, the uncertainty term is ignored in the current study as discussed earlier in section 2.

The plausibility of this assumption is justified when considering the zonal gradients obtained for unperturbed quiet days with mainly low gradients as is shown in Figure 5. Here the regular pattern of the diurnal variation of less than 5 mTECU/km (0.8 mm/km at L1) can be seen clearly although the values are rather small and far from being crucial for precise positioning or safety of life applications. This result is confirmed by GIX, GIXS, and $GIXP_{95}$ values over these days as shown in Figure 6 where the gradient values are averaged over the area (30–70°N; 20°W–50°E).

The ability to monitor rather small regular gradients associated with the regular diurnal variation of the ionospheric ionization in the order of 1–3 mm/km (Lee et al., 2006) strongly supports the applicability of the suggested indices to characterize the perturbation degree of the ionosphere.

3.1.2. Perturbed Conditions

Ionospheric perturbations are of interest in GNSS applications if spatial gradients exceed certain threshold value or if the protection level monitoring of ionospheric storms indicates that the performance of GNSS navigation and positioning applications degrades. Here the GIX analysis is presented for the Halloween storm in October/November 2003 and the St. Patrick's Day storm in March 2015. Both geomagnetic storms and their related ionospheric effects are considered in numerous publications (e.g., Borries et al., 2016; Zakharenkova et al., 2016). Therefore, this paper only focuses on signatures which can be seen in the GIX analysis.

To illustrate the capability of selecting different scales in GIX, both the GIX and GIXS components were plotted for two different scales in Figure 7 for the severe Halloween storm over Europe from 29 October to 11 November 2003 (data bound is 30–70°N; 20°W–50° E). The dipole length may vary between 30 and 250 km (top left panel) and between 50 and 500 km (top right panel).

In the lower panel, the large-scale effects are pronounced with characteristic scales between 50 and 500 km. It is remarkable that South-North and West-East components show different features at different scales, pronouncing gradients in North-South direction by a factor of 2 compared with the West-East direction. It is

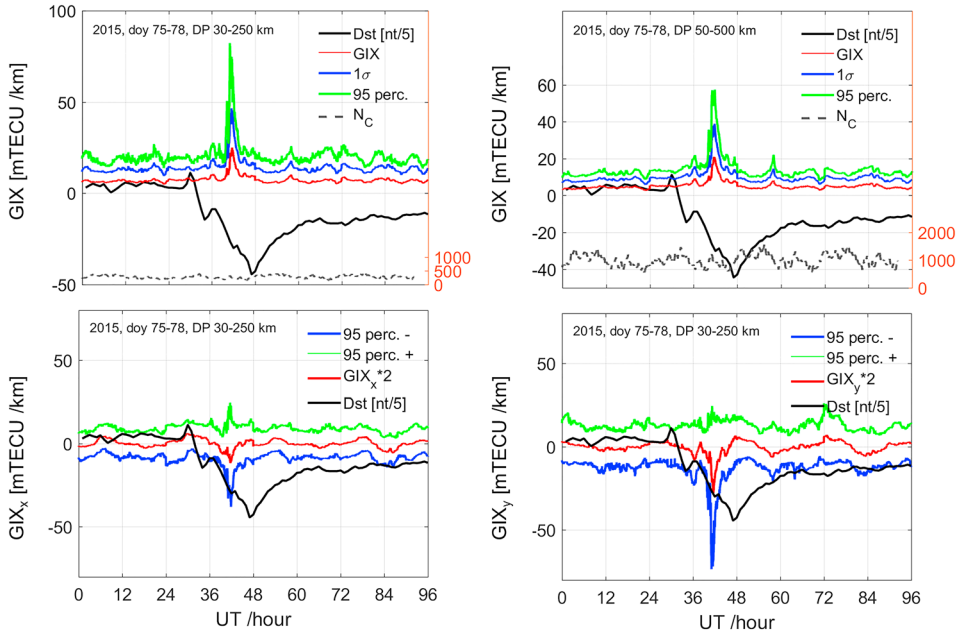

Figure 8. GIX, GIX Sigma, and $GIXP_{95}$ analysis for 16–20 March 2015 (St. Patrick's Day storm) at ranges 30–250 and 50–500 km (top panels). Components of GIX and $GIXP_{95\pm}$ over Europe (30–70° N; 20° W–50° E) in comparison with the geomagnetic Dst index for 30-250 km range (bottom panels). Mean gradient values are multiplied by 2 and Dst index is divided by 5 for better visibility. GIX = Gradient Ionosphere indeX.

worth mentioning that the larger scale provides lower and smoother perturbation indices, for example, up to 60 mTECU/km for GIXS (80 mTECU/km for $GIXP_{95}$) instead of approximately 80 mTECU/km (140 mTECU/km for $GIXP_{95}$) shown at the shorter range. This is also in agreement with essentially stronger smoothing over longer distances. Therefore, where data coverage allows, the dipole length range should be as short as possible. Here the number of dipoles considered N_C reduces from approximately 600 for 50–500 km to approximately 100 for the 30–250-km range (top panel in Figure 7).

As expected, GIXS is correlated with the Dst index to a certain extent, but it does show well pronounced individual characteristics. This clearly supports the idea that geomagnetic indices like Kp and Dst cannot describe ionospheric features in a detail that is directly usable by customers. The ionospheric plasma is subjected to a number of influencing factors such as perturbation electric fields, thermospheric winds, plasmaspheric fluxes, or composition changes all of which modulate the ionospheric perturbation processes causing quite different behavior to that shown in Dst. During the severe storm in question, the American Wide Area Augmentation System failed for several hours because the vertical error limit of 50 m was exceeded. Specific ionospheric indices are essential for estimating the impact of ionospheric perturbations on GNSS applications.

The next sample presented in Figure 8 shows GIX estimates over mid-Europe (30–70°N; 20°W–50°E) during the St. Patrick's Day storm for dipole length ranges of 30–250 and 50–500 km. The St. Patrick's Day storm was described in many papers reporting several types of ionospheric perturbations (e.g., Borries et al., 2016; Zakharenkova et al., 2016). The Storm Sudden Commencement was reported to occur at approximately 04:45 UT, whereas the auroral activity index AE shows two peaks at approximately 09:00 and 14:00 UT. As shown in Figure 8, the ionospheric effects can be seen approximately 3 hr later at approximately 12:00 and 17:00 UT in the area under consideration. It is obvious that the highest ionospheric dynamics seen in the South-North as well as in the West-East component appears during the growth phase of the geomagnetic storm and not in the Dst minimum. This is an interesting finding that seems to be a general feature for mid-latitude ionospheric storms (cf. Wilken et al., 2018) and, therefore, requires more detailed studies for clarification.

Furthermore, we see quite different results of GIX, GIXS, and $GIXP_{95}$ for different dipole length ranges. The higher values of gradients have been computed for the shorter range (30–250 km, $N_C \approx 250$) than for the

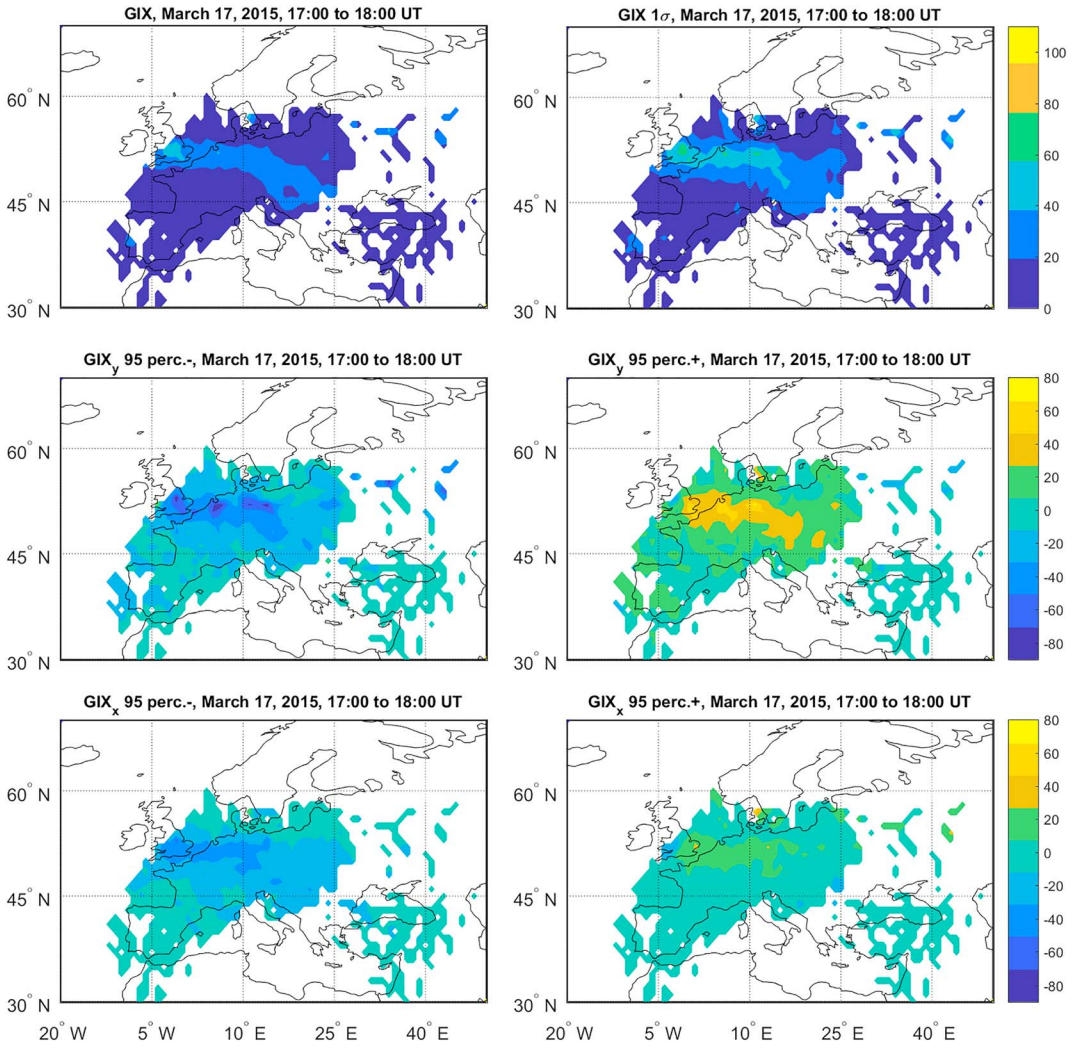

Figure 9. European maps of GIX, GIX Sigma, and $GIXP_{95}$ components averaged over 1 hr between 17:00 and 18:00. The dipole length range is with 50–1,000 km rather large to obtain sufficient data coverage for mapping. GIX = Gradient Ionosphere indeX.

longer range (50–500 km, $N_C \approx 1{,}000$). It is interesting to note that else at the Halloween storm $GIXP_{95-}$ and $GIXP_{95+}$ (lower panels) are strongly asymmetric indicating the occurrence of an ionospheric front. As the enhanced negative South-North gradient and the asymmetry of $GIXP_{95\pm}$ show, there is a strong enhancement of TEC at lower latitudes within the considered Mid-European area (30–70°N; 20°W–50°E) on 17 March 2015. This is indicated in Figure 9 where maps of GIX, GIXS, and $GIXP_{95\pm}$ components are shown after averaging the indices within the time period of 17:00 and 18:00 UT.

The performance of the European Geostationary Navigation Overlay Service (EGNOS) station Aalborg (57° N, 10° E) during the St. Patrick's Day storm on 17 March 2015, made available by the EGNOS Service Provider, is considered to check the applicability of GIX, GIXS, and $GIXP_{95}$. Space weather-induced perturbations of the ionosphere may lead to a degradation of SBAS like EGNOS. The Vertical Protection Level (VPL) is measured and represents the upper bound of the position error. If this value exceeds a certain upper limit, for example, of 50 m, SBAS is not available for aircraft landing. As Figure 10 shows, EGNOS VPL (green curve) was clearly affected by ionospheric perturbations associated with the St. Patrick's Day storm. The most disturbed period of the EGNOS station Aalborg (57° N, 10° E) fits quite well with the peak values of the derived GIX, GIXS, and $GIXP_{95}$ although these indices are representative for the rather large surrounding area of Aalborg to keep the number of observations above 100. Thus, based on GIX monitoring, a nowcast warning could have been issued to customers like EGNOS.

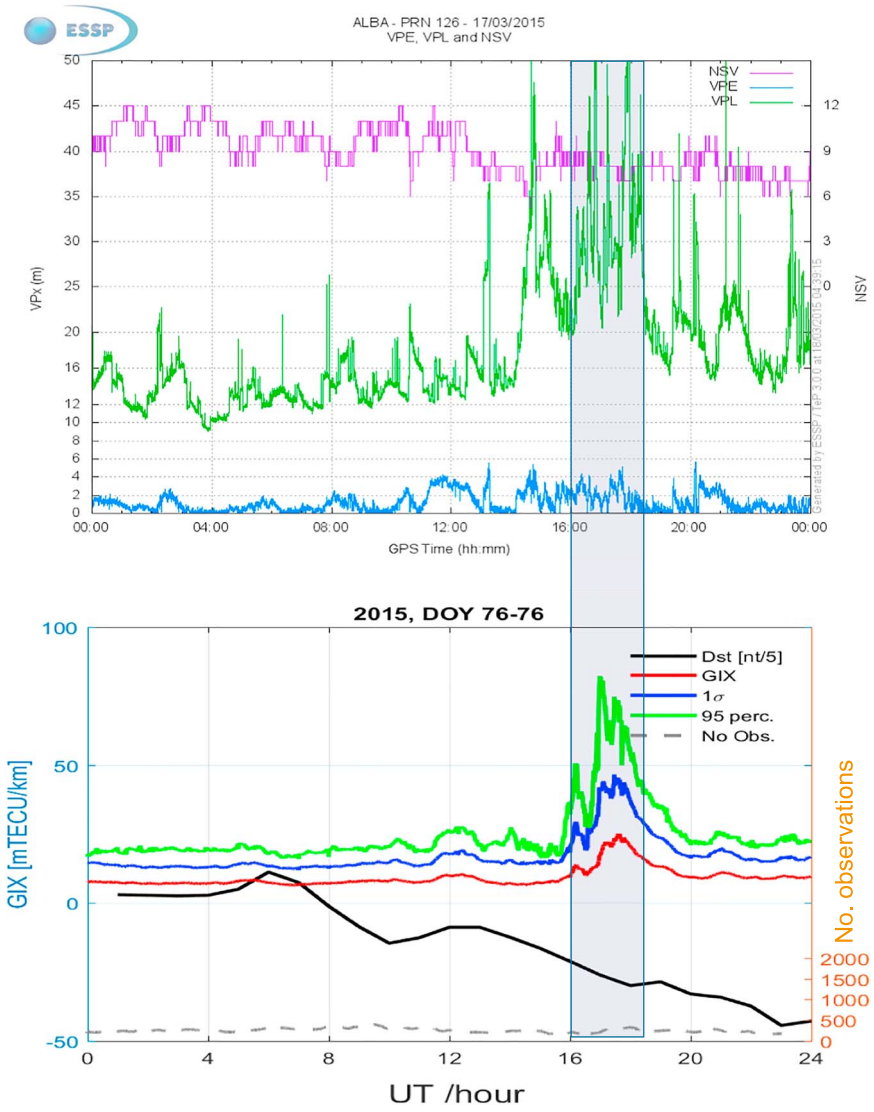

Figure 10. EGNOS system performance derived by the EGNOS Service Provider for the EGNOS station Aalborg (57°N, 10°E; top) in comparison with perturbation indices GIX, GIX Sigma, and $GIXP_{95}$ over Europe (30–70° N; 20° W–50° E, dipole range 30–250 km) and the geomagnetic Dst index. NSV (pink): Number of satellites used to generate the EGNOS navigation solution; VPE (blue): 95th percentile of vertical positioning error; VPL (green): 95th percentile of vertical protection level. NSV= Number of Space Vehicles; VPE=Vertical Protection Error, VPL = Vertical Protection Level; GIX = Gradient Ionosphere indeX; EGNOS = European Geostationary Navigation Overlay Service.

As Figure 10 shows, $GIXP_{95}$ is nearly twice as much GIXS (1σ) which indicates that GIXP has the potential to be closer to extreme gradient values which are crucial for positioning.

Furthermore, the 95th percentile corresponds quite well with the positioning estimates of EGNOS. Because the derived GIX values refer to a large area over Europe (30–70° N; 20° W–50° E), the local measurements at Aalborg may indicate some additional local disturbances as it seems to be the case between 13:00–16:00 and 19:00–00:00 UT. On the other hand, the enhanced VPL and VPE values might be caused by a bad satellite geometry given by low Number of Space Vehicles (NSV) values (only 6–7 satellites available).

3.2. Temporal Estimates by SIDX

Rapid changes of TEC may lead to instantaneous range errors of several meters in GNSS applications (Jakowski, 2017). Extreme fast enhancements of the plasma density resulting on sharp increases of TEC may be caused by intense solar flares (Hernández-Pajares et al., 2012) or energetic particle precipitation (Jayachandran et al., 2012), for example. As such instantaneous events cannot be reliably predicted at

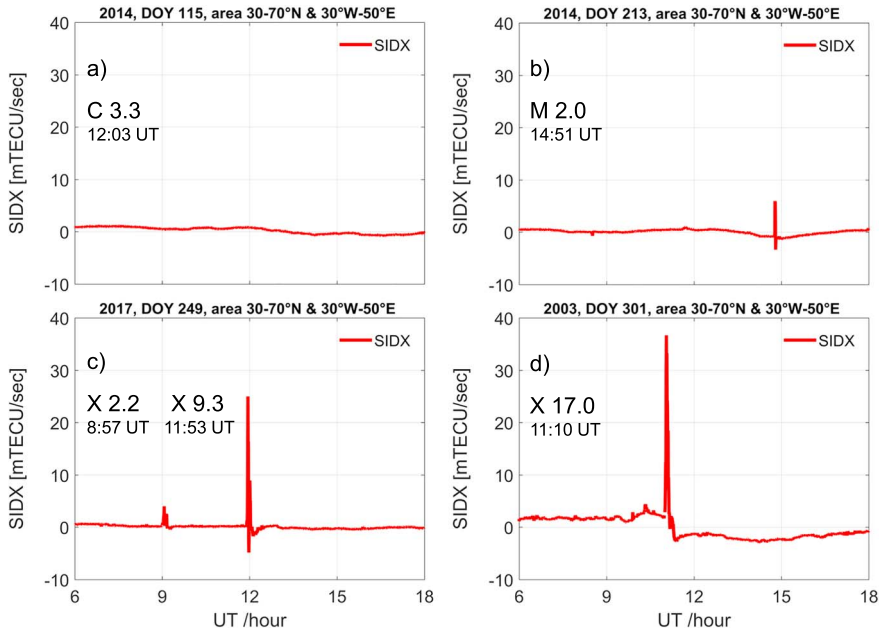

Figure 11. SIDX monitoring results obtained for days with solar flare effects detected by GOES. (a) 25 April 2014, C 3.3 flare at 12:03 UT (not detected by SIDX). (b) 1 August 2014, M 2.0 flare at 14:51 UT. (c) 6 September 2017 X 2.2 and X 9.3 flare at 08:57 UT and 11:53 UT respectively. (d) 28 October 2003, X 17.0 flare at 11:10 UT. SIDX = Sudden Ionospheric Disturbance indeX.

present, customers need clear information regarding the time and intensity of such events in near real-time to estimate potential risks in a realistic way and to avoid false risk estimates.

Current flare detection systems measure high energetic X-ray fluxes in wavelength ranges 0.1–0.8 nm or detect/measure ionospheric signatures by using amplitude and phase measurements of Very Low Frequency radio waves from military transmitters (Wenzel et al., 2016). This information can be directly used in High Frequency (HF) communication because X-rays ionize the bottomside ionosphere and therefore, impact terrestrial HF communication. Space-based radio systems used in satellite communication, navigation, and remote sensing radars are more sensitive to the total electron content between satellite and receiver. Therefore, these customers primarily need information on solar flares whose extreme ultraviolet percentage on the total spectrum is high. The extreme ultraviolet radiation at wavelengths <130 nm ionizes the most frequent oxygen atoms in the F2 layer.

After simulating the capability of the proposed SIDX to detect solar flares here, the capability is checked with real data. In Figure 11, SIDX results are shown for four different days where flares ware recorded by the Geostationary Operational Environmental Satellite (GOES) X-ray detectors.

According to these few samples, solar flares whose amplitude exceeds the C level have a good chance at being recorded using the SIDX technique. However, it must also be stated that due to the spectral variety of solar flares, there is no fixed relationship between the SIDX amplitude with X-ray flares classified by GOES. An investigation into such relationships requires further study.

In Figure 12, the impact of a solar X9.3 flare monitored via SIDX on the Precise Point Positioning (PPP) service is shown for single (green line) and dual frequency (red line) positioning (cf. Berdermann et al., 2018). The solar flare started at 11:53 UT and peaked at 12:02 UT on 6 September 2017 which is clearly indicated by SIDX in both of the top panels. The uppermost panel shows that the flare impacts all latitudes in view. The bottom panel shows the associated deviation of the PPP service at a selected IGS station from reference coordinates in meters calculated in 30-s intervals for East, North, and in the vertical direction. Obviously, SIDX has clearly exceeded a critical value that may indicate problems in solving phase ambiguity. As a first step, the $\lambda/2$ level at L1 frequency was marked as a crucial value when using 30-s data. Further studies are needed to quantify critical thresholds for customers in order to define a user-friendly SIDX scale. If phase ambiguity solution is lost, PPP needs a longer convergence time to

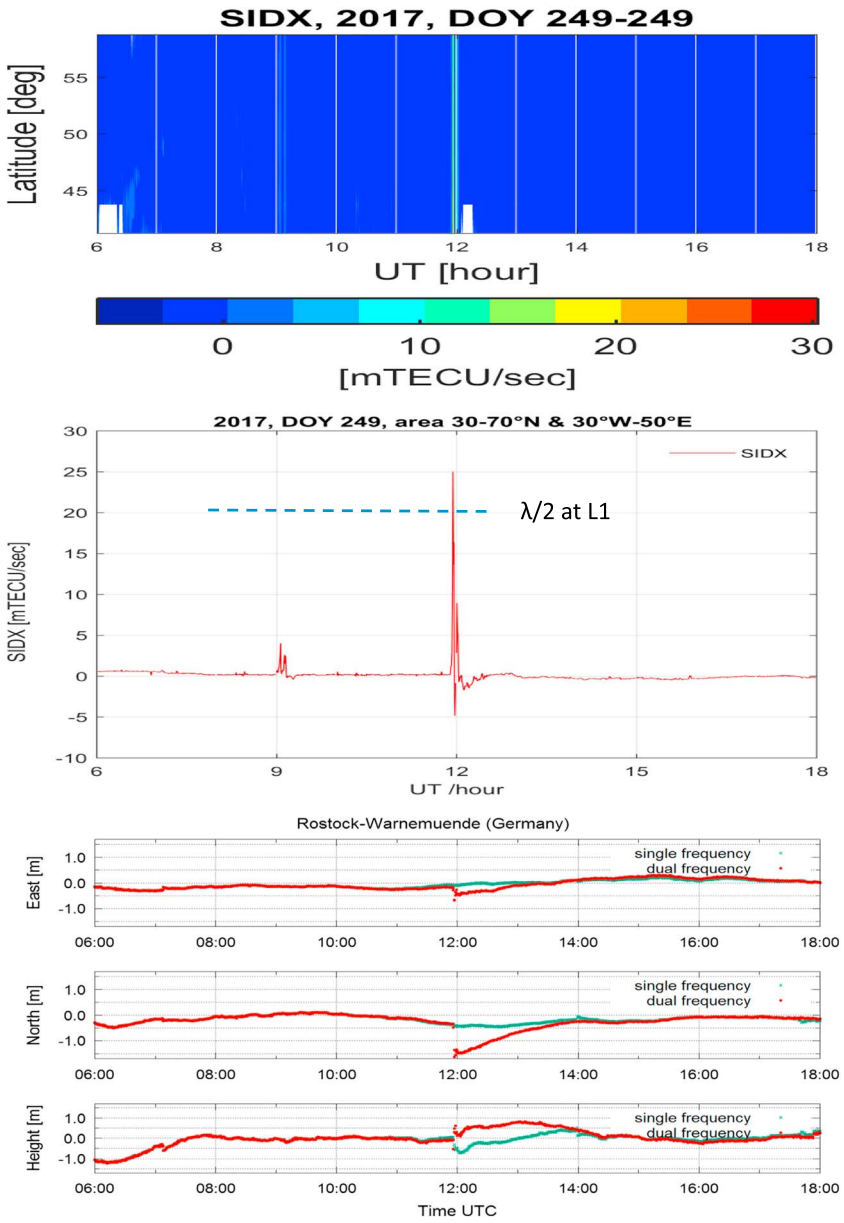

Figure 12. SIDX detection of a X9.3 solar flare on 6 September 2017 over Europe (top panels). Impact of the X9.3 flare on single and dual frequency Precise Point Positioning accuracy at the IGS station WARN (φ: 54.17 N; λ: 12.10 E) in Rostock-Warnemünde (Germany) on 6 September 2017 (cf. Berdermann et al., 2018). SIDX = Sudden Ionospheric Disturbance indeX.

estimate the phase ambiguities as can be seen in the lower panel of Figure 12 (for further details, see Berdermann et al., 2018). In any case, early information regarding solar flare events helps to estimate the technical consequences on operational PPP services.

4. Conclusions

Precision and safety of life applications of GNSS require supplementary information on space weather conditions, in particular regarding the perturbation degree of the ionosphere. To estimate the potential of spatial gradients and rapid temporal variations of ionospheric TEC being crucial to precision and safety of life applications, two approaches were discussed. The advantage of these approaches is their capability to estimate the perturbation degree of the ionosphere instantaneously without statistical analyses of

historical data, that is, without taking into account previous measurements. This advantage makes the suggested indices attractive for space weather services providing actual information in near real-time. A disadvantage of GIX indices might be that the computations require calibrated STEC data. At present state-of-the-art TEC, calibration achieves an accuracy of approximately 1 TECU along satellite-receiver links. The capabilities and accuracy of the index approaches were demonstrated in simulations using a 3-D electron density model of the ionosphere and plasmasphere in conjunction with realistic GNSS constellations. Their applicability was tested using real data sets of GNSS measurements at midlatitudes. The ability to estimate even very small spatial gradients of a quiet midlatitude ionosphere confirms the applicability of GIX and derived quantities such as GIXS and $GIXD_{95}$ to monitor the direction and location of spatial gradients that might be crucial for precise positioning and Safety of Life applications of GNSS in near real-time. GIX and SIDX estimates at lower latitudes in particular near the equatorial crests will provide much higher values compared with those considered in this paper. It is expected that phenomena like ionospheric bubbles can more often result in high GIX values being crucial for precision and safety of life applications.

Continuous monitoring of proposed indices has the potential to not only estimate the strength of ionospheric fronts but also the propagation direction and velocity, that is, to also predict their arrival at specific locations such as airports.

Compared with Station-Pair and Single-Station methods reported in the literature, the method proposed here for defining spatial ionospheric perturbation indices benefits from the improved statistical database at each epoch resulting from the combination of all available or specifically selected ionospheric piercing points. The number of piercing points can remarkably be enlarged when a multi-GNSS constellation is included in the computations. For example, compared with GPS with an orbit inclination of 55°, the inclusion of GLONASS will improve the data availability especially at high latitudes due to the higher inclination of 60°.

The potential of these approaches to serve as objective ionospheric indices for scaling horizontal TEC gradients and rapid solar flare effects has been shown. Thus, a near real-time provision of proposed index approaches should be well suited to reducing safety and accuracy risk in GNSS navigation and positioning. To utilize this potential, more comprehensive studies are needed to analyze ionospheric storms under different solar-terrestrial conditions using GNSS measurements.

Acknowledgments
We would like to thank the International GNSS service and the associated community for providing high quality GNSS data used for analysis. We would like to give thanks to sponsors and operators of NASA's Earth Science Data Systems and the CDDIS for archiving and distributing the IGS data. We are grateful to the EGNOS Service Provider (ESSP) for making the performance estimates of EGNOS available to us, as well as Anja Heßelbart for providing the PPP results for 6 September 2017. All data used within the publication are available from the long-term storage of the Institute of Communication and Navigation of the German Aerospace Center and are permanently provided via ftp access (Server: ftp.kn.nz.dlr.de/AGU_SW_Jakowski_Hoque_2018, User: dlr79, Password: 7uN3LaBZhebv) or on request to the email address (impc-uhd@dlr.de).

References

Berdermann J., Jakowski, N., Hoque, M. M., Hlubek, N., Missling, K. D., Kriegel, M., et al. (2014). Ionospheric Monitoring and Prediction Center (IMPC), Proceedings of the 27th International Technical Meeting of the Satellite Division of the Institute of Navigation (ION GNSS+ 2014), Tampa, Florida, September 2014 (pp. 14–21).

Berdermann, J., Kriegel, M., Banyś, D., Heymann, F., Hoque, M. M., Wilken, V., et al. (2018). Ionospheric response to the X9.3 flare on 6 September 2017 and its implication for navigation services over Europe. *Space Weather*, *16*, 1604–1615. https://doi.org/10.1029/2018SW001933

Borries, C., Mahrous, A. M., Ellahouny, N. M., & Badeke, R. (2016). Multiple ionospheric perturbations during the Saint Patrick's Day storm 2015 in the European-African sector. *Journal of Geophysical Research: Space Physics*, *121*, 11, 333–11,345. https://doi.org/10.1002/2016JA023178

Hernández-Pajares, M., García-Rigo, A. J., Juan, J. M., Sanz, J., Monte, E., & Aragón-Àngel, A. (2012). GNSS measurement of EUV photons flux rate during strong and mid solar flares. *Space Weather*, *10*, S12001. https://doi.org/10.1029/2012SW000826

Hoque, M. M., & Jakowski, N. (2011). A new global empirical NmF2 model for operational use in radio systems. *Radio Science*, *46*, RS6015. https://doi.org/10.1029/2011RS004807

Hoque, M. M., & Jakowski, N. (2012). A new global model for the ionospheric F2 peak height for radio wave propagation. *Annales de Geophysique*, *30*(5), 797–809. https://doi.org/10.5194/angeo-30-797-2012

Hoque, M. M., N. Jakowski, & J. Berdermann (2014). A new approach for mitigating ionospheric mapping function errors. ION GNSS+ 2014, 8.-12. Sep. 2014, Tampa, USA.

Jakowski, N. (2017). Ionosphere monitoring. In *Springer handbook of global navigation satellite systems* (pp. 1139–1162). Verlag: Springer. 978-3-319-4292926-7

Jakowski, N., Béniguel, Y., De Franceschi, G., De, G., Hernandez-Pajares, M., Jacobsen, K. S., et al. (2012). Monitoring, tracking and forecasting ionospheric perturbations using GNSS techniques. *Journal of Space Weather and Space Climate*, *2*, A22. https://doi.org/10.1051/swsc/2012022

Jakowski, N., Borries, C., & Wilken, V. (2012). Introducing a disturbance ionosphere index (DIX). *Radio Science*, *47*, RS0L14. https://doi.org/10.1029/2011RS004939

Jakowski, N., & Hoque, M. M. (2018). A new electron density model of the plasmasphere for operational applications and services. *Journal of Space Weather and Space Climate*, *8*, A16. https://doi.org/10.1051/swsc/2018002

Jakowski, N., Hoque, M. M., & Mayer, C. (2011). A new global TEC model for estimating trans-ionospheric radio wave propagation errors. *Journal of Geodesy*, *85*(12), 965–997. https://doi.org/10.1007/s00190-011-0455-1

Jakowski, N., & Lazo, B. (1977). Die Auswirkungen von Solar Flares auf die Messung der Gesamtelektronenzahl am Beispiel von ATS-6-Beobachtungen. *Physics Solariterr.*, *6*, 51–58.

Jakowski, N., Mayer, C., Hoque, M. M., & Wilken, V. (2011). Total electron content models and their use in ionosphere monitoring. *Radio Science*, *46*, RS0D18. https://doi.org/10.1029/2010RS004620

Jakowski, N., Stankov, S. M., Schlueter, S., & Klaehn, D. (2005). On developing a new ionospheric perturbation index for space weather operations. *Advances in Space Research*, *38*(11), 2596–2600. https://doi.org/10.1016/j.asr.2005.07.043

Jayachandran, P. T., Hosokawa, K., Shiokawa, K., Otsuka, Y., Watson, C., Mushini, S. C., et al. (2012). GPS total electron content variations associated with poleward moving Sun-aligned arcs. *Journal of Geophysical Research*, *117*, A05310. https://doi.org/10.1029/2011JA017423

Lee, J., Pullen, S., Datta-Barua, S., & Enge, P. (2006). Assessment of nominal ionosphere spatial decorrelation for LAAS. https://doi.org/10.1109/PLANS.2006.1650638

Mannucci, A. J., Tsurutani, B. T., Iijima, B. A., Komjathy, A., Saito, A., Gonzalez, W. D., et al. (2005). Dayside global ionospheric response to the major interplanetary events of October 29–30, 2003 "Halloween storms". *Geophysical Research Letters*, *32*, L12S02. https://doi.org/10.1029/2004GL021467

Mayer, C., Belabbas, B., Jakowski, N., Meurer, M., & Dunkel, W. (2009). Ionosphere Threat Space Model Assessment for GBAS, In: Proc. ION GNSS 2009, 22.-25. Sep. 2009, Savannah, GA, USA.

Montenbruck, O., Hauschild, A., & Steigenberger, P. (2014). Differential code bias estimation using multi-GNSS observations and global ionosphere maps. *Navigation*, *61*(3), 191–201. https://doi.org/10.1002/navi.64

Pi, X., Mannucci, A. J., Lindqwister, U. J., & Ho, C. M. (1997). Monitoring of global ionospheric irregularities using the worldwide GPS network. *Geophysical Research Letters*, *24*(18), 2283–2286. https://doi.org/10.1029/97GL02273

Pradipta, R., & Doherty, P. H. (2016). Assessing the occurrence pattern of large ionospheric TEC gradients over the Brazilian airspace. *Navigation*, *63*(3), 335–343. https://doi.org/10.1002/navi.141

Pullen, S., Park, Y. S., & Enge, P. (2009). Impact and mitigation of ionosphere anomalies on ground-based augmentation of GNSS. *Radio Science*, *44*, RS0A21. https://doi.org/10.1029/2008RS004084

Saito, S., Sunda, S., Lee, J., Pullen, S., Supriadi, S., Yoshihara, T., et al. (2017). Ionospheric delay gradient model for GBAS in the Asia-Pacific region. *GPS Solutions*, *21*(4), 1937–1947. https://doi.org/10.1007/s10291-017-0662-1

Sanz J., Juan, J., González-Casado, G., Prieto-Cerdeira, R., Schlüter, S., & Orús, R. (2014). Novel ionospheric activity indicator specifically tailored for GNSS users, Proc. of the 27th International Technical Meeting of the Satellite Division of the Institute of Navigation (ION GNSS+ 2014), Tampa, Florida, September 2014 (pp. 1173–1182).

Weber, G., Dettmering, D., & Gebhard, H. (2005). Networked Transport of RTCM via Internet Protocol (NTRIP). In F. Sansò (Ed.), *A Window on the Future of Geodesy. International Association of Geodesy Symposia* (Vol. 128). Berlin: Springer. https://doi.org/10.1007/3-540-27432-4_11

Wenzel, D., Jakowski, N., Berdermann, J., Mayer, C., Valladares, C., & Heber, B. (2016). Global Ionospheric Flare Detection System (GIFDS). *Journal of Atmospheric and Solar-Terrestrial Physics*, *138–139*, 233–242. https://doi.org/10.1016/j.jastp.2015.12.011

Wilken, V., Kriegel, M., Jakowski, N., & Berdermann, J. (2018). An ionospheric index suitable for estimating the degree of ionospheric perturbations. *Journal of Space Weather and Space Climate*, *8*, A19. https://doi.org/10.1051/swsc/2018008

Zakharenkova, I., Astafyeva, E., & Cherniak, I. (2016). GPS and GLONASS observations of large-scale traveling ionospheric disturbances during the 2015 St. Patrick's Day storm. *Journal of Geophysical Research: Space Physics*, *121*, 138–12,156. https://doi.org/10.1002/2016JA023332